Step-Flow Growth of Graphene-Boron Nitride Lateral Heterostructures by Molecular Beam Epitaxy

James Thomas[1], Jonathan Bradford[1], Tin S. Cheng[1], Alex Summerfield[1], James Wrigley[1], Christopher J. Mellor[1], Andrei N. Khlobystov[2], C. Thomas Foxon[1], Laurence Eaves[1], Sergei V. Novikov[1] and Peter H. Beton[1]

[1]*School of Physics & Astronomy, University of Nottingham, Nottingham, NG7 2RD, UK*

[2]*School of Chemistry, University of Nottingham, Nottingham, NG7 2RD, UK*

Corresponding author: peter.beton@nottingham.ac.uk

Abstract

Integration of graphene and hexagonal boron nitride (hBN) into lateral heterostructures has drawn focus due to the ability to broadly engineer the material properties. Hybrid monolayers with tuneable bandgaps have been reported, while the interface itself possesses unique electronic and magnetic qualities. Herein, we demonstrate lateral heteroepitaxial growth of graphene and hBN by sequential growth using high-temperature molecular beam epitaxy (MBE) on highly ordered pyrolytic graphite (HOPG). We find, using scanning probe microscopy, that graphene growth nucleates at hBN step edges and grows across the surface to form nanoribbons with a controlled width that is highly uniform across the surface. The graphene nanoribbons grow conformally from the armchair edges of hexagonal hBN islands forming multiply connected regions with the growth front alternating from armchair to zigzag in regions nucleated close to the vertices of hexagonal hBN islands. Images with lattice resolution confirm a lateral epitaxial alignment between the hBN and graphene nanoribbons, while the presence of a moiré pattern within the ribbons indicates that some strain relief occurs at the lateral heterojunction. These results demonstrate that high temperature MBE is a viable route towards integrating graphene and hBN in lateral heterostructures.

Introduction

The use of hexagonal boron nitride (hBN) as a supporting substrate for high quality graphene results in striking improvements in carrier mobility and device performance[1–3]. The advantages of hBN arise, in part, from its atomically flat terraces, its low lattice mismatch with graphene (approximately 1.8 %), and its isostructural hexagonal crystal lattice. In addition, graphene/hBN heterostructures have interesting structural properties including commensurate-incommensurate stacking[4], and quantum effects such as the introduction of a graphene bandgap[5], the fractional quantum Hall effect[6,7], and the formation of Hofstadter's butterfly electronic statesat large magnetic fields[8–10]. Furthermore, van der Waals heterostructures formed by placing few-layer hBN between graphene contacts can be used as tunnelling transistors[11–15], with many additional possibilities when used in combination with other two-dimensional (2D) materials[11,16].

Despite the increasing interest in graphene/hBN heterostructures, the direct growth of graphene on hBN is relatively uncommon and most graphene/hBN vertical heterostructures consist of stacks of layers mechanically exfoliated from bulk material[17]. The growth of vertical structures by chemical vapour deposition (CVD), in which a layer of graphene is formed on top of hBN appears problematic and has been reported by only a few groups[3,18–21]. Owing to the small lattice mismatch it is also possible to incorporate graphene and hBN in a lateral heterostructure[3,22]. The hybrid monolayer has been predicted to possess a widely tuneable electronic bandgap [23,24], while an atomically precise interface between graphene and hBN can host novel electronic and magnetic states[25–27]. In short, the properties of the lateral heterostructure are dictated by the size, geometry and interface structure of hBN and graphene domains. There has been progress in growing lateral heterostructures using CVD[3,28–33] or direct chemical conversion of graphene layers[34,35]. These efforts have culminated in the fabrication of atomically thin devices[36] and circuitry[37] constructed from laterally connected hBN and graphene layers.

We have recently investigated the growth of graphene and hBN using high-temperature molecular beam epitaxy (MBE) and demonstrated that this is a viable approach, resulting in monolayers and heterostructures with properties that have not, to date, been realised in CVD-grown materials. For example, graphene grown on hBN by MBE has residual tensile strain and can even be lattice-matched with the hBN substrate[38,39], while a crossover to a direct band gap has been observed in MBE-grown hBN monolayers on highly oriented pyrolytic graphite (HOPG), accompanied by photoluminescence in the deep ultra-violet region of the spectrum[40–42].

In this paper we present the sequential high-temperature MBE growth of hBN and graphene and show that this leads to lateral heterostructures, principally through step-flow growth. First, hBN is grown on HOPG using plasma-assisted MBE, with the nucleation of hBN growth primarily at steps on the graphite substrate. This is followed by the MBE growth of graphene using an electron beam carbon source. In some cases, hBN/HOPG samples are directly transferred to a second MBE chamber for graphene growth, while others are investigated *ex situ* using atomic force microscopy (AFM) after hBN growth, before re-introduction to the MBE system. Graphene grown in both cases nucleates at step edges of epitaxially-grown hBN, and grows laterally across the surface to form graphene nanoribbons, with a width which is highly uniform and tuneable across the substrate surface.

Experimental

To grow hBN on HOPG we followed similar protocols to those described previously [41,42]; HOPG substrates (1 x 1 cm^2) were cleaned by heating to 400 ^oC for approximately 8 hours in an Ar/H_2 (95:5) atmosphere and then transferred to a custom-designed high-temperature dual chamber GENxplor MBE system operating under ultra-high vacuum (UHV) conditions (base pressure ~ 10^{-10} mbar). hBN was then grown by plasma-assisted MBE at a substrate temperature of 1390 ^oC , with a high-temperature Veeco effusion cell operated at 1875 ^oC to sublime boron, and a conventional Veeco radio-frequency (RF) plasma source to generate the active nitrogen flux; this was operated at an N_2

flow of 2 sccm and an RF power of 550 W. A growth time of 3 hours was used, resulting in hBN covering over ~80% of the HOPG substrate surface.

The hBN/HOPG samples were cooled to room temperature and transferred within the UHV system to the graphene MBE growth chamber. In some cases, the samples were removed temporarily from the UHV system in order to acquire images of their morphology using atomic force microscopy (AFM) allowing a direct comparison of regions of the surface before and after graphene growth; these samples were then returned to the MBE system for graphene growth. In our previous work[38,39], carbon was deposited using a heated graphitic filament in a SUKO63 source, but here we use a vertical electron beam evaporator EBVV 63-T4, fitted with a high purity carbon anode target; both sources are produced by Dr. Eberl MBE-Komponenten GmbH. During growth the e-beam current was increased to, typically, 300 mA, with a ramp rate of 10 mA/min, and held at this value during the growth time (up to a several minutes), then ramped down at a rate of 100 mA/min. The accelerating voltage was 5 kV and the substrate temperature was 1390 ^{o}C for all samples. This method of growth has allowed for more controlled deposition compared to the carbon filament source, due to the increased stability and tunability of the e-beam source.

AFM and conductive AFM (cAFM) images were acquired under ambient conditions using an Asylum Research Cypher-S instrument with a mixture of NuNano Scout 70 and Spark 70 Pt (for cAFM) probes, and Budget Sensors MultiAl-75 and ElectriMulti75-G (for cAFM) probes. Conductive AFM measurements were recorded with a -50 mV bias applied to the sample. Topographic images were acquired in both AC (tapping) and contact mode; in contact mode, the deflection channel allows for clear identification of step edges, while in tapping mode the phase channel is found to provide good contrast between hBN and graphene. STM images were acquired using an Agilent Technologies 4500 PicoPlus STM instrument in ambient conditions with mechanically formed PtIr tips. The bias voltage is applied to the tip with the sample grounded. Image processing was performed using the Gwyddion software package[43].

Results and Discussion

Figure 1 shows a direct comparison of the morphology of a specific area of an HOPG substrate on which a near monolayer of hBN has been grown both before (a-c) and after (d-f) subsequent graphene growth. AFM images of the surface acquired *ex situ* before graphene growth show that hBN has grown laterally across the HOPG surface from three-dimensional aggregates which are formed, primarily at HOPG step edges[41,44]. The hBN is revealed in contact mode deflection channel images, panels a) and c), and topographic maps (panel b). From the topography image in panel b) we determine the layer thickness (see inset); the hBN layer number and regions of uncovered areas of the HOPG substrate are labelled in panel a). Islands of hBN nucleated at different points form separate domains that merge as the surface coverage increases. The boundaries between domains are difficult to resolve in topographic images but appear more clearly in the deflection images a) and c), with one such boundary highlighted in c). In these areas there are many hBN step edges as well as partially formed hexagonal bilayer and multilayer hBN islands. This morphology is very similar to that reported in our previous studies of the MBE growth of hBN on HOPG[41,44,45].

This particular sample (hBN on HOPG) was returned to the MBE system and, after growth of graphene, further AFM images of the same area were acquired (Figs. 1d-f). In comparison with Figs. 1a-cWe observe additional features at the edge of the hexagonal partial hBN island at the centre of Fig. 1d. These are also present in the topographic image Fig. 1e but are resolved much more clearly in Fig. 1f. This phase image provides contrast between different materials and we attribute the brighter strip around the edges of the hBN island to graphene which has nucleated at the hBN step edge and grown outward across the surface. The profile in Fig. 1e inset shows that there is a very small variation in apparent height across the boundary between the hBN and the graphene strip as expected for such a growth mode (see regions identified by red arrows; the hBN/graphene boundaries are highlighted by white arrows in Fig. 1e and the accompanying profile). This lateral growth is observed at every hBN island and step edge.

We also observe topographically bright features in Fig. 1e at the graphene/hBN lateral interface; these are attributed to graphitic aggregates, commonly seen in MBE growth[39,46] of graphene. In some cases these clusters provide the nucleation site for higher layers of graphene. In addition, isolated islands of graphene nucleated on hBN at sites remote from step edges are observed, for example the island in the lower right of Figs. 1e and 1f (marked by a red arrow).

A comparison of Figs. 1a and 1d also reveals the presence of meandering linear features, which were not resolved in Fig. 1a; these correspond to regions where graphene growth has been nucleated at hBN domain boundaries. The presence of this additional graphene is also shown clearly close to the domain boundary identified in Fig. 1c; compare with the higher resolution images of the same area in Fig. 1e (topographic) and Fig. 1f (phase).

The graphene strips form a lateral heterojunction with the hBN from which they grow and are reminiscent of graphene nanoribbons which are formed using molecular self-assembly and on-surface polymerisation[47], as well as analogous structures which have been grown using CVD[30]. These lateral graphene-hBN heterointerfaces are explored in further detail in the remainder of this paper.

Figure 2 shows a lateral heterostructure formed by sequentially growing hBN and graphene without removal of the sample from UHV environment of the MBE system. Figure 2a shows a topographic image close to the edge of an hBN island which is predominantly of monolayer height (topographic region marked 1), but also has several regions of second (marked 2) and higher layers of hBN. In addition, a region of HOPG, which remained uncovered exposed after hBN growth, is present on the left-hand side of the image. Figure 2b shows a conductive AFM (cAFM) image of the same region. In this mode an AFM tip with a conductive coating is scanned in contact mode across the surface, while applying a potential difference between tip and sample and recording the resultant current.

In the cAFM images the lower region to the left-hand-side of the topography image Fig. 2a, is the exposed HOPG substrate, showing up as highly conducting in Fig. 2b in which bright/dark contrast corresponds to high/low current. The monolayer hBN terrace on the right-hand-side of the image, appears darker (less conductive) but there are two raised hexagonal islands identified as bi-layer hBN islands in the topographic image Fig. 2a. Graphene nanoribbon growth (G) can be seen along all hBN step edges within these images and appears with bright contrast in the cAFM images. This is particularly clear for the graphene which has grown around the second layer hBN islands. Nanoribbon growth is also evident at the edges of the more disordered hBN multilayer on the centre-right of these images. In addition, graphene grows across HOPG from the edge of the first layer hBN; this is evident from the contrast variation in Fig. 2a. Overall, we do not observe significant differences between samples which are imaged *ex-situ* after first stage of hBN growth and returned to the MBE system, and those which are transferred to the second MBE chamber within UHV without *ex-situ* AFM prior to graphene growth.

The widths of the graphene bands shown in Figs. 1 and 2 appear to have a high degree of uniformity, with measured widths of 30 nm and 80 nm, respectively. A more systematic analysis of widths of graphene is provided for three samples grown with different amounts of deposited carbon in Figure 3. The graphene in Fig. 3a was grown by ramping the carbon source e-beam current to 280 mA with a rate of 10 mA/min before immediately ramping down with a rate of 100 mA/min. For the samples shown in Figs. 3b and 3c the current was ramped up to 300 mA, at the same rate, before being ramped down either immediately (b) or after 1 minute (c). The histogram in Fig. 3d shows the collated measurements of graphene widths determined by AFM for these three samples and two additional samples grown with the same conditions as the sample shown in Fig. 3c. As the amount of deposited carbon increases, the graphene width systematically increases from 18 ± 4 nm (Fig. 3a) to 29 ± 4 nm (Fig. 3b) to 83±11 nm (Fig. 3c). In each case the variance of the distribution is significantly smaller than the mean width. These measurements confirm that the graphene widths for a given set of growth conditions have a narrow distribution and systematically increase with increased

deposition time/carbon flux, confirming the potential tunability of the width of the graphene nanoribbons grown using this approach.

The uniformity of the graphene width is also evident through the conformal relationship between the growing edge of the graphene and the hBN step edge morphology from which it nucleated, i.e. the graphene edges follow (and are nearly parallel to) the shape of the hBN edges. An interesting exception is revealed close to the vertices where hBN facets meet. An example is shown in the topographic image in Fig. 3e (a zoom of the region highlighted by the red square in Fig. 3b); here the growing edges of graphene are approximately parallel to the hBN island edge, but an additional facet evolves close to the hBN apex at an angle of, approximately, 30° to the hBN edge.

We attribute this facet to the evolution of a zigzag (ZZ) edge, which, as expected, is at 30^{o} to the hBN edges, which are attributed to armchair edges, due to the hexagonal island shape. This is illustrated schematically in Fig. 3f. According to numerical modelling of graphene edges the armchair edge is expected to have a lower energy than the zigzag termination [48]. However, it has also known zigzag edges can undergo a reconstruction thereby reducing their energy [48]. In addition, a zigzag termination has been observed to evolve at the edges of holes in graphene under electron bombardment [49]. The energetics are thus likely to depend critically on experimental conditions such as temperature and substrate, but the transition to a zigzag edge close to hBN vertices was observed consistently across our samples. Note that hBN islands terminated by either N- or B-terminated ZZ edges are expected to have a triangular shape for ZZ favourable edges[50], whereas under our growth conditions hexagonal islands are formed.

This assignment has been confirmed using lattice resolution imaging of a hexagonal hBN island bounded by graphene bands (see cAFM image in Figure 4a; the inset showing the corresponding topographic image). Figures 4b and 4c present lattice resolution images of the graphene and hBN lattices at the locations indicated in Fig. 4a. Figure 4b is a 10 nm cAFM image, whereas Fig. 4c is a 5 nm lateral force image. The lattice directions have been extracted from a 2D Fourier transform and

are indicated by the red (graphene) and black/white (hBN) arrows in Fig. 4. The hexagonal island edges, along with the parallel graphene edges, run at 30° to the lattice direction confirming the edges to be armchair terminated, whereas the additional graphene edges are parallel to the lattice direction confirming a ZZ termination. Furthermore, these images confirm the epitaxial relationship between the hBN island and the growing graphene. Figure 4a also demonstrates the merging of two graphene domains growing from separate hBN islands. Images of this region, acquired with lattice resolution, show a defect-free merging of the two bands with no obvious domain boundary.

One of the unique features of graphene grown on hBN using high-temperature MBE[38,39] is the intrinsic strain, which results in moiré wavelengths larger than that expected for relaxed graphene aligned to the hBN lattice. Moiré patterns with different wavelengths have been observed in cAFM and STM images of graphene strips with sufficiently large width. Figures 5a and 5b show STM images of graphene, which has grown from the edge of an hBN monolayer across the HOPG substrate, and from the edge of a hBN bilayer. In the STM images the hBN layers appear in darker contrast compared to the laterally connected graphene regions, similar to the contrast observed in cAFM. The images were recorded with a tip bias within the bandgap of hBN and as such the tunnelling current is established between the STM tip and the HOPG substrate. In order to maintain the tunnelling current, the tip is extended closer to the surface to give an inverted tip-height contrast for the hBN layers.

Due to the lattice mismatch between graphene and hBN, moiré patterns arise in areas where both graphene and hBN are present in the heterostructure. In Fig. 5a, no moiré patterns are seen in the graphene strip extending over HOPG from the edge of the first hBN layer, indicating that this region is unstrained and aligned to the underlying HOPG lattice. A prominent moiré pattern with a wavelength, λ, of 17.1 nm is observed in the second hBN layer (marked as 2L hBN/HOPG). The expected hBN/graphene moiré pattern has a maximum wavelength of ~14nm for unstrained, rotationally aligned material. The longer moiré wavelength may be due to compressive strain of the

hBN lattice by approximately 0.35% due to the underlying HOPG substrate. Though a moiré pattern is not clearly resolved on the hBN monolayer (marked as 1L hBN/HOPG) in Fig. 5a, it can be routinely imaged under different tunnelling conditions (see Figure S1(a), Supplementary Information which shows a moiré wavelength of 18.4 nm), or by cAFM[45].

Figure 5a also shows graphene bands, grown from the edges of two hexagonal BN bilayers, which have seamlessly merged. On the graphene there is a moiré pattern which was measured to have λ = 17.2 nm from the line profile shown in Fig. 5b. This closely matches the moiré wavelength in the hBN region, which suggests that the graphene layer is locally unstrained or minimally strained. Where the graphene band laterally extends onto the graphene ribbon supported by HOPG, there is an abrupt disappearance of the moiré pattern, marked with a red arrow in Figs. 5a and 5b, indicating that the graphene is unstrained and lattice matched to the underlying graphene and HOPG. It is noted that the moiré wavelength is not uniform in all regions of the graphene band, which suggests non-uniform strain. The non-uniformity is highlighted in a different ribbon shown in Fig. 5c, where a short moiré wavelength of 13.5 nm exists along one edge of the hBN domain, and a longer wavelength of 25.2 nm is observed along the bottom edge (line profiles shown in Fig. 5d). The short moiré pattern would correspond to relaxed graphene and hBN layers with a small rotational misalignment (~0.25°), whereas the longer wavelength would correspond to tensile strain of 0.81% in the graphene strip. We can further demonstrate that the moiré patterns arise due to tensile strain in the graphene band by imaging stress relaxation after tearing the ribbon with the STM tip (see Figure S1d,e, Supplementary Information). Interestingly, there seems to be a sharp boundary between the two regions originating at the corner of the hBN island in Fig. 5c and this may suggest that the lattice strain is influenced by the hBN/graphene lateral interface. Finally, we note that moiré patterns were not observed in narrower graphene ribbons, where the width is comparable to the expected moiré wavelength (see Figure S1a, Supplementary Information).

In the images acquired to date we have been unable to resolve the atomic detail of the structure very close to (within ~ 1 nm) the interfacial boundary between hBN and graphene. This is likely due to the presence of defects as well as electron scattering due to the interface itself [51] which is known to complicate the local density of states and, thus, the apparent topography as determined by STM. We have also investigated these samples using Raman spectroscopy (data are shown in Figure S2 Supplementary Information), but, in agreement with our previous work [41], the spectral region close to the hBN $E2g$ peak is dominated by the D peak from the underlying graphite.

Conclusions

It is clear from the above results that in high-temperature MBE at the growth temperature 1390 ^{o}C graphene grows preferentially laterally from the edges of hBN in a mode of step-flow growth, which results in the formation of lateral graphene-hBN heterojunctions. The graphene and hBN regions show a clear epitaxial relationship through the alignment of atomic lattices. However, the variations in strain for different regions revealed by different, and locally-varying, moiré periods suggest small differences of lattice constant in the graphene and hBN regions. These differences are likely to be relieved by defects in the interfacial regions[52,53]. The morphology of the graphene is somewhat different to that observed in the MBE growth on exfoliated hBN flakes for which the step density is very low[39]. The epitaxial hBN on HOPG studied here has a much higher density of steps, including those around hexagonal hBN islands, which are not observed on exfoliated flakes. Growth around the hexagonal hBN islands provide a route to the formation multiply connected regions of graphene and in addition leads to a free edge, which alternates between armchair and zigzag terminations. Interestingly, a complementary structure of hBN strips grown around a hexagonal graphene island using chemical vapour deposition has recently reported, but with much larger dimensions [54]. Preservation of the edge termination during sequential MBE growth could lead to selective growth of oriented lateral hBN-graphene heterointerfaces, which possess novel electronic and magnetic

properties[26]. Most importantly, in this mode of growth the width of the graphene strips shows a high degree of uniformity across the hBN, offering the prospect of controllable growth of graphene rings and nano-strips with dimensions small enough to lead to measurable quantum confinement and magnetic flux quantisation effects. Our results show clearly that high-temperature MBE provides a route to the formation of lateral heterojunctions and novel in-plane heterostructures between graphene and hBN.

Acknowledgements

This work was supported by the Engineering and Physical Sciences Research Council UK [Grant number EP/P019080/1]. P.H.B thanks the Leverhulme Trust for the award of a Research Fellowship [RF-2019-460].

Data Availability

The image files on which the figures in this paper are based are available at doi 10.17639/nott.7040

References

[1] Dean C R, Young A F, Meric I, Lee C, Wang L, Sorgenfrei S, Watanabe K, Taniguchi T, Kim P, Shepard K L and Hone J 2010 Boron nitride substrates for high-quality graphene electronics. *Nat. Nanotechnol.* **5** 722–6

[2] Gannett W, Regan W, Watanabe K, Taniguchi T, Crommie M F and Zettl A 2011 Boron nitride substrates for high mobility chemical vapor deposited graphene *Appl. Phys. Lett.* **98** 242105

[3] Li Q, Liu M, Zhang Y and Liu Z 2016 Hexagonal Boron Nitride-Graphene Heterostructures: Synthesis and Interfacial Properties *Small* **12** 32–50

[4] Woods C R, Britnell L, Eckmann A, Ma R S, Lu J C, Guo H M, Lin X, Yu G L, Cao Y, Gorbachev R V., Kretinin A V, Park J, Ponomarenko L A, Katsnelson M I, Gornostyrev Y N, Watanabe K, Taniguchi T, Casiraghi C, Gao H, Geim A K and Novoselov K S 2014 Commensurate–incommensurate transition in graphene on hexagonal boron nitride *Nat. Phys.* **10** 451–6

[5] Hunt B, Sanchez-Yamagishi J D, Young A F, Yankowitz M, LeRoy B J, Watanabe K, Taniguchi T, Moon P, Koshino M, Jarillo-Herrero P and Ashoori R C 2013 Massive Dirac Fermions and Hofstadter Butterfly in a van der Waals Heterostructure *Science* **340** 1427–30

[6] Bolotin K I, Ghahari F, Shulman M D, Stormer H L and Kim P 2009 Observation of the fractional quantum Hall effect in graphene *Nature* **462** 196–9

[7] Du X, Skachko I, Duerr F, Luican A and Andrei E Y 2009 Fractional quantum Hall effect and insulating phase of Dirac electrons in graphene *Nature* **462** 192–5

[8] Wallbank J R, Mucha-Kruczyński M, Chen X and Fal'ko V I 2015 Moiré superlattice effects in graphene/boron-nitride van der Waals heterostructures *Ann. Phys.* **376** 359–76

[9] Dean C R, Wang L, Maher P, Forsythe C, Ghahari F, Gao Y, Katoch J, Ishigami M, Moon P, Koshino M, Taniguchi T, Watanabe K, Shepard K L, Hone J and Kim P 2013 Hofstadter's butterfly and the fractal quantum Hall effect in moiré superlattices *Nature* **497** 598–602

[10] Ponomarenko L A, Gorbachev R V, Yu G L, Elias D C, Jalil R, Patel A A, Mishchenko A, Mayorov A S, Woods C R, Wallbank J R, Mucha-Kruczynski M, Piot B A, Potemski M, Grigorieva I V, Novoselov K S, Guinea F, Fal'ko V I and Geim A K 2013 Cloning of Dirac fermions in graphene superlattices. *Nature* **497** 594–7

[11] Yankowitz M, Xue J and LeRoy B J 2014 Graphene on hexagonal boron nitride *J. Phys. Condens. Matter* **26** 303201

[12] Britnell L, Gorbachev R V, Jalil R, Belle B D, Schedin F, Mishchenko A, Georgiou T, Katsnelson M I, Eaves L, Morozov S V, Peres N M R, Leist J, Geim A K, Novoselov K S and Ponomarenko L A 2012 Field-effect tunneling transistor based on vertical graphene heterostructures. *Science* **335** 947–50

[13] Chen B, Huang H, Ma X, Huang L, Zhang Z and Peng L M 2014 How good can CVD-grown monolayer graphene be? *Nanoscale* **6** 15255–61

[14] Mishchenko A, Tu J S, Cao Y, Gorbachev R V, Wallbank J R, Greenaway M T, Morozov V E, Morozov S V, Zhu M J, Wong S L, Withers F, Woods C R, Kim Y-J, Watanabe K, Taniguchi T, Vdovin E E, Makarovsky O, Fromhold T M, Fal'ko V I, Geim A K, Eaves L and Novoselov K S 2014 Twist-controlled resonant tunnelling in graphene/boron nitride/graphene heterostructures *Nat. Nanotechnol.* **9** 808–13

[15] Fallahazad B, Lee K, Kang S, Xue J, Larentis S, Corbet C, Kim K, Movva H C P, Taniguchi T,

Watanabe K, Register L F, Banerjee S K and Tutuc E 2015 Gate-tunable resonant tunneling in double bilayer graphene heterostructures *Nano Lett.* **15** 428–33

[16] Novoselov K S, Mishchenko A, Carvalho A and Castro Neto A H 2016 2D materials and van der Waals heterostructures *Science* **353** aac9439

[17] Geim A K and Grigorieva I V 2013 Van der Waals heterostructures. *Nature* **499** 419–25

[18] Zhang C, Zhao S, Jin C, Koh A L, Zhou Y, Xu W, Li Q, Xiong Q, Peng H and Liu Z 2015 Direct growth of large-area graphene and boron nitride heterostructures by a co-segregation method *Nat. Commun.* **6** 6519

[19] Lu G, Wu T, Yang P, Yang Y, Jin Z, Chen W, Jia S, Wang H, Zhang G, Sun J, Ajayan P M, Lou J, Xie X and Jiang M 2017 Synthesis of High-Quality Graphene and Hexagonal Boron Nitride Monolayer In-Plane Heterostructure on Cu-Ni Alloy *Adv. Sci.* **4** 1700076

[20] Tang S, Wang H, Wang H S, Sun Q, Zhang X, Cong C, Xie H, Liu X, Zhou X, Huang F, Chen X, Yu T, Ding F, Xie X and Jiang M 2015 Silane-catalysed fast growth of large single-crystalline graphene on hexagonal boron nitride *Nat. Commun.* **6** 6499

[21] Yang W, Chen G, Shi Z, Liu C-C, Zhang L, Xie G, Cheng M, Wang D, Yang R, Shi D, Watanabe K, Taniguchi T, Yao Y, Zhang Y and Zhang G 2013 Epitaxial growth of single-domain graphene on hexagonal boron nitride. *Nat. Mater.* **12** 792–7

[22] Ci L, Song L, Jin C, Jariwala D, Wu D, Li Y, Srivastava A, Wang Z F, Storr K, Balicas L, Liu F and Ajayan P M 2010 Atomic layers of hybridized boron nitride and graphene domains *Nat. Mater.* **9** 430–5

[23] Fan X, Shen Z, Liu A Q and Kuo J L 2012 Band gap opening of graphene by doping small boron nitride domains *Nanoscale* **4** 2157–65

[24] Wang J, Zhao R, Liu Z and Liu Z 2013 Widely Tunable Carrier Mobility of Boron Nitride-Embedded Graphene *Small* **9** 1373–8

[25] Liu Y, Bhowmick S and Yakobson B I 2011 BN White Graphene with “Colorful” Edges: The Energies and Morphology *Nano Lett.* **11** 3113–6

[26] Bhowmick S, Singh A K and Yakobson B I 2011 Quantum dots and nanoroads of graphene embedded in hexagonal boron nitride *J. Phys. Chem. C* **115** 9889–93

[27] Drost R, Uppstu A, Schulz F, Hämäläinen S K, Ervasti M, Harju A and Liljeroth P 2014 Electronic States at the Graphene–Hexagonal Boron Nitride Zigzag Interface *Nano Lett.* **14** 5128–32

[28] Liu Z, Song L, Zhao S, Huang J, Ma L, Zhang J, Lou J and Ajayan P M 2011 Direct growth of graphene/hexagonal boron nitride stacked layers *Nano Lett.* **11** 2032–7

[29] Liu L, Park J, Siegel D A, McCarty K F, Clark K W, Deng W, Basile L, Idrobo J C, Li A-P and Gu G 2014 Heteroepitaxial Growth of Two-Dimensional Hexagonal Boron Nitride Templated by Graphene Edges *Science* **343** 163–7

[30] Sutter P, Huang Y and Sutter E 2014 Nanoscale integration of two-dimensional materials by lateral heteroepitaxy *Nano Lett.* **14** 4846–51

[31] Lu J, Zhang K, Feng Liu X, Zhang H, Chien Sum T, Castro Neto A H and Loh K P 2013 Order–disorder transition in a two-dimensional boron–carbon–nitride alloy *Nat. Commun.* **4** 2681

[32] Gao Y, Zhang Y, Chen P, Li Y, Liu M, Gao T, Ma D, Chen Y, Cheng Z, Qiu X, Duan W and Liu Z

2013 Toward single-layer uniform hexagonal boron nitride-graphene patchworks with zigzag linking edges *Nano Lett.* **13** 3439–43

[33] Camilli L, Jørgensen J H, Tersoff J, Stoot A C, Balog R, Cassidy A, Sadowski J T, Bøggild P and Hornekær L 2017 Self-assembly of ordered graphene nanodot arrays *Nat. Commun.* **8** 47

[34] Bradford J, Shafiei M, MacLeod J and Motta N 2019 Transfer-Free Synthesis of Lateral Graphene–Hexagonal Boron Nitride Heterostructures from Chemically Converted Epitaxial Graphene *Adv. Mater. Interfaces* **6** 1900419

[35] Gong Y, Shi G, Zhang Z, Zhou W, Jung J, Gao W, Ma L, Yang Y, Yang S, You G, Vajtai R, Xu Q, MacDonald A H, Yakobson B I, Lou J, Liu Z and Ajayan P M 2014 Direct chemical conversion of graphene to boron- and nitrogen- and carbon-containing atomic layers *Nat. Commun.* **5** 3193

[36] Liu Z, Ma L, Shi G, Zhou W, Gong Y, Lei S, Yang X, Zhang J, Yu J, Hackenberg K P, Babakhani A, Idrobo J C, Vajtai R, Lou J and Ajayan P M 2013 In-plane heterostructures of graphene and hexagonal boron nitride with controlled domain sizes *Nat. Nanotechnol.* **8** 119–24

[37] Levendorf M P, Kim C J, Brown L, Huang P Y, Havener R W, Muller D A and Park J 2012 Graphene and boron nitride lateral heterostructures for atomically thin circuitry *Nature* **488** 627–32

[38] Davies A, Albar J D, Summerfield A, Thomas J C, Cheng T S, Korolkov V V., Stapleton E, Wrigley J, Goodey N L, Mellor C J, Khlobystov A N, Watanabe K, Taniguchi T, Foxon C T, Eaves L, Novikov S V. and Beton P H 2018 Lattice-Matched Epitaxial Graphene Grown on Boron Nitride *Nano Lett.* **18** 498–504

[39] Summerfield A, Davies A, Cheng T S, Korolkov V V., Cho Y, Mellor C J, Foxon C T T, Khlobystov A N, Watanabe K, Taniguchi T, Eaves L, Novikov S V. and Beton P H 2016 Strain-Engineered Graphene Grown on Hexagonal Boron Nitride by Molecular Beam Epitaxy *Sci. Rep.* **6** 22440

[40] Elias C, Valvin P, Pelini T, Summerfield A, Mellor C J, Cheng T S, Eaves L, Foxon C T, Beton P H, Novikov S V., Gil B and Cassabois G 2019 Direct band-gap crossover in epitaxial monolayer boron nitride *Nat. Commun.* **10** 2639

[41] Cho Y-J, Summerfield A, Davies A, Cheng T S, Smith E F, Mellor C J, Khlobystov A N, Foxon C T T, Eaves L, Beton P H and Novikov S V. 2016 Hexagonal Boron Nitride Tunnel Barriers Grown on Graphite by High Temperature Molecular Beam Epitaxy *Sci. Rep.* **6** 34474

[42] Vuong T Q P, Cassabois G, Valvin P, Rousseau E, Summerfield A, Mellor C J, Cho Y, Cheng T S, Albar J D, Eaves L, Foxon C T, Beton P H, Novikov S V and Gil B 2017 Deep ultraviolet emission in hexagonal boron nitride grown by high-temperature molecular beam epitaxy *2D Mater.* **4** 021023

[43] Nečas D and Klapetek P 2011 Gwyddion: an open-source software for SPM data analysis *Cent. Eur. J. Phys.* **10** 181–8

[44] Cheng T S, Summerfield A, Mellor C J, Davies A, Khlobystov A N, Eaves L, Foxon C T, Beton P H and Novikov S V. 2018 High-temperature molecular beam epitaxy of hexagonal boron nitride layers *J. Vac. Sci. Technol. B* **36** 02D103

[45] Summerfield A, Kozikov A, Cheng T S, Davies A, Cho Y Y-J, Khlobystov A N, Mellor C J, Foxon C T, Watanabe K, Taniguchi T, Eaves L, Novoselov K S, Novikov S V. and Beton P H 2018 Moiré-Modulated Conductance of Hexagonal Boron Nitride Tunnel Barriers *Nano Lett.* **18** 4241–6

[46] Albar J D, Summerfield A, Cheng T S, Davies A, Smith E F, Khlobystov A N, Mellor C J, Taniguchi T, Watanabe K, Foxon C T, Eaves L, Beton P H and Novikov S V 2017 An atomic

carbon source for high temperature molecular beam epitaxy of graphene *Sci. Rep.* **7** 6598

[47] Cai J, Ruffieux P, Jaafar R, Bieri M, Braun T, Blankenburg S, Muoth M, Seitsonen A P, Saleh M, Feng X, Müllen K and Fasel R 2010 Atomically precise bottom-up fabrication of graphene nanoribbons. *Nature* **466** 470–3

[48] Koskinen P, Malola S and Häkkinen H 2008 Self-Passivating Edge Reconstructions of Graphene *Phys. Rev. Lett.* **101** 115502

[49] Girit C O, Meyer J C, Erni R, Rossell M D, Kisielowski C, Yang L, Park C-H, Crommie M F, Cohen M L, Louie S G and Zettl A 2009 Graphene at the Edge: Stability and Dynamics *Science* **323** 1705–8

[50] Stehle Y Y, Sang X, Unocic R R, Voylov D, Jackson R K, Smirnov S and Vlassiouk I 2017 Anisotropic Etching of Hexagonal Boron Nitride and Graphene: Question of Edge Terminations *Nano Lett.* **17** 7306–14

[51] Rutter G M, Crain J N, Guisinger N P, Li T, First P N and Stroscio J A 2007 Scattering and Interference in Epitaxial Graphene *Science* **317** 219–22

[52] Lu J, Gomes L C, Nunes R W, Castro Neto A H and Loh K P 2014 Lattice relaxation at the interface of two-dimensional crystals: Graphene and hexagonal boron-nitride *Nano Lett.* **14** 5133–9

[53] Nandwana D and Ertekin E 2015 Ripples, strain, and misfit dislocations: Structure of graphene-boron nitride superlattice interfaces *Nano Lett.* **15** 1468–75

[54] Geng D, Dong J, Kee Ang L, Ding F and Yang H Y 2019 In situ epitaxial engineering of graphene and h-BN lateral heterostructure with a tunable morphology comprising h-BN domains *NPG Asia Mater.* **11** 56

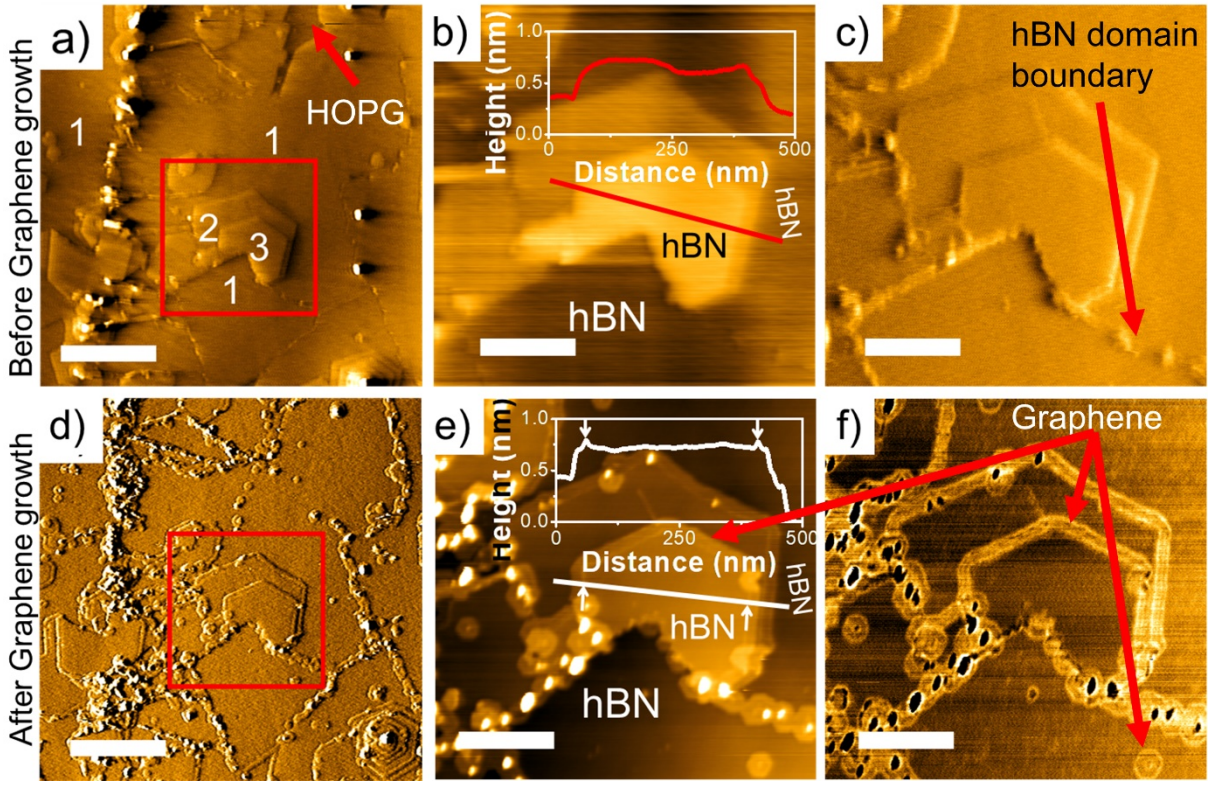

Figure 1: a) Contact mode deflection image of hBN grown on HOPG with a surface coverage >80%. The numbers indicate the hBN layer, from monolayer (1) to trilayer (3); a region of HOPG is also marked. b) and c) show contact mode topography and deflection maps respectively of the region bounded by the red box in a). A profile along the red line in b) is shown in the inset. d) Deflection image of the same region as a), measured after graphene growth. Figures e) and f) show topographic and phase channels acquired in AC mode of the region within the red box in d), both recorded following graphene growth. The phase image provides contrast between the graphene and hBN regions, highlighting graphene growth at hBN step edges, domain boundaries, and isolated graphene islands. A profile along the white line in e) is shown in the inset. Scalebars: 500 nm in a) and d), and 200 nm in b), c), e) and f).

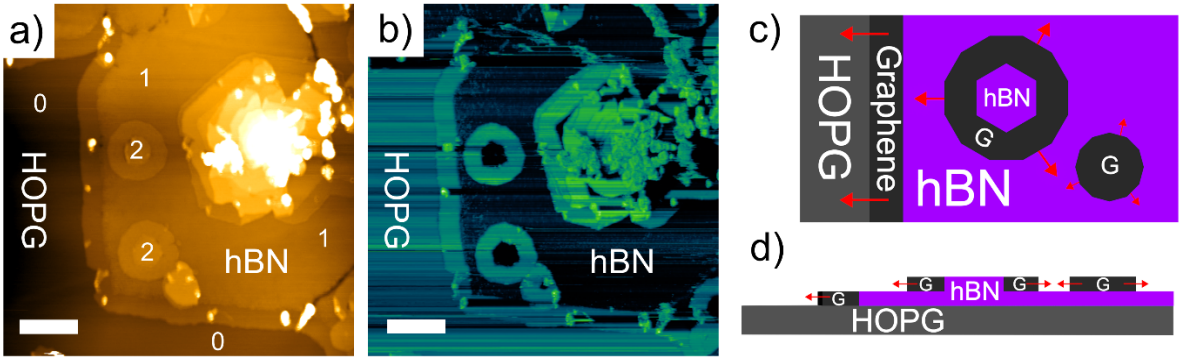

Figure 2: Images of a sample grown without removal from the MBE system. a) and b) show AFM images recorded in AC mode (a) and conductive mode (b). The number of hBN layers present are indicated in a). The current scale in b) ranges from 0 to 9.4 µA. The scalebars are 250 nm in both a) and b). The graphene bands are clearly visible in the current image, b). Figures c) and d) show a top-down and cross-sectional schematic respectively of the sample structure. MBE graphene growth (G) at hBN step edges, on HOPG and surrounding hBN islands, are shown alongside growth of graphene only islands. The in-plane lateral direction of graphene step flow growth is highlighted by the arrows.

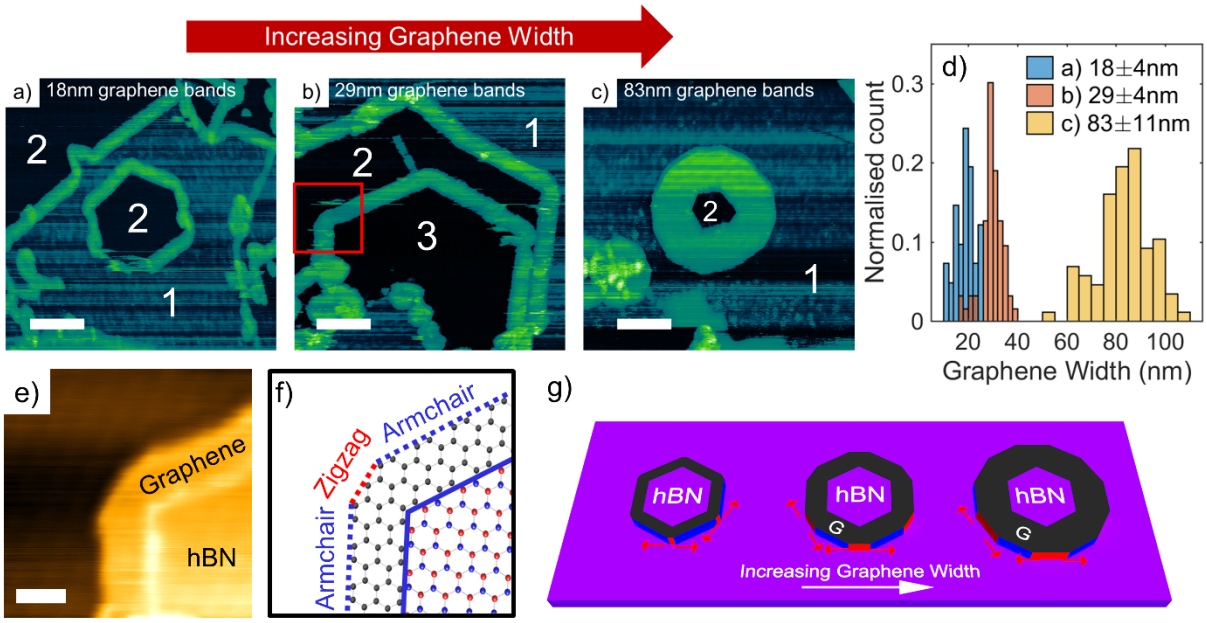

Figure 3: a-c) Three cAFM current images recorded on three separate samples with varying growth conditions with increasing graphene widths from left to right. Current values ranging from 0 to 1.5 µA, 2.5 µA, 2.7 µA in a), b), and c) respectively. The numbers indicate the number of hBN layers, from monolayer (1) to trilayer (3). d) shows the recorded distribution for graphene band widths. 41 measurements were made across the sample shown in figure a), 63 measurements across the sample shown in figure b), and 87 measurements spread across 3 samples with the growth conditions of the sample shown in figure c). e) An AC topography image of the region bounded by the red square in b). In this figure the additional zigzag graphene edge appearing at the hBN corners can be clearly seen. Figure f) shows a schematic representation of figure e) with the expected lattice termination types indicated. Figure g) shows a diagram indicating the graphene growth with extended amount of deposited carbon. The blue edges indicate armchair termination, and the red edges indicate zigzag termination in both f) and g). At longer growth times the zigzag edges (red) become elongated, as the graphene bands become thicker. Scalebars are 100 nm in a) to c), and 25 nm in e).

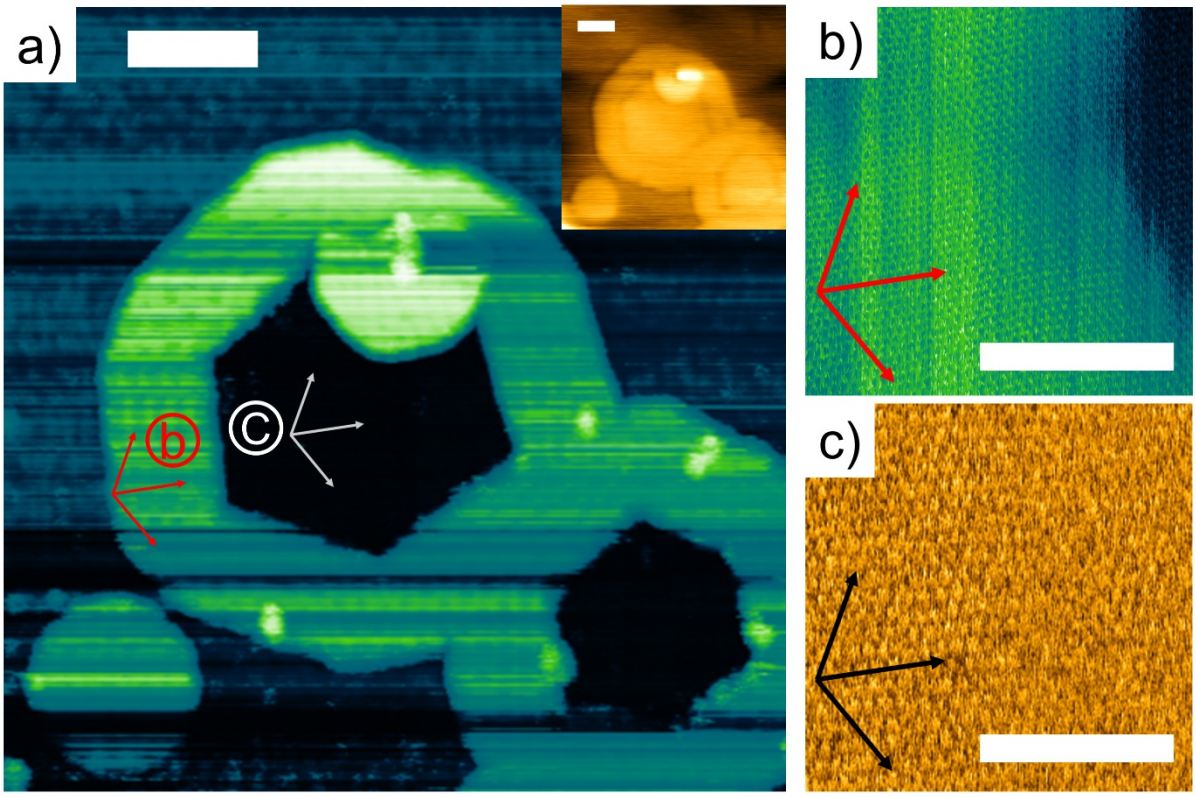

Figure 4: a) a cAFM current image showing 75 nm graphene bands with a current scale ranging from 0 to 1.1 µA. An approximately 18 nm moiré pattern can be seen on the graphene. The inset shows a contact topography image of the same region. b) lattice resolution cAFM image recorded on the graphene region indicated in a. The red arrows indicate the lattice directions as determined from a 2D Fourier transform of the image. Similarly, c) shows a lattice resolution lateral force image recorded on the hBN region indicated in a), with the black arrows (white in a)) indicating the lattice directions. These images confirm the armchair edge type for the hBN islands, and armchair/zigzag terminations of the graphene edges. Scalebars are 100 nm in a) and a) inset, 5 nm in b), and 2.5 nm in c).

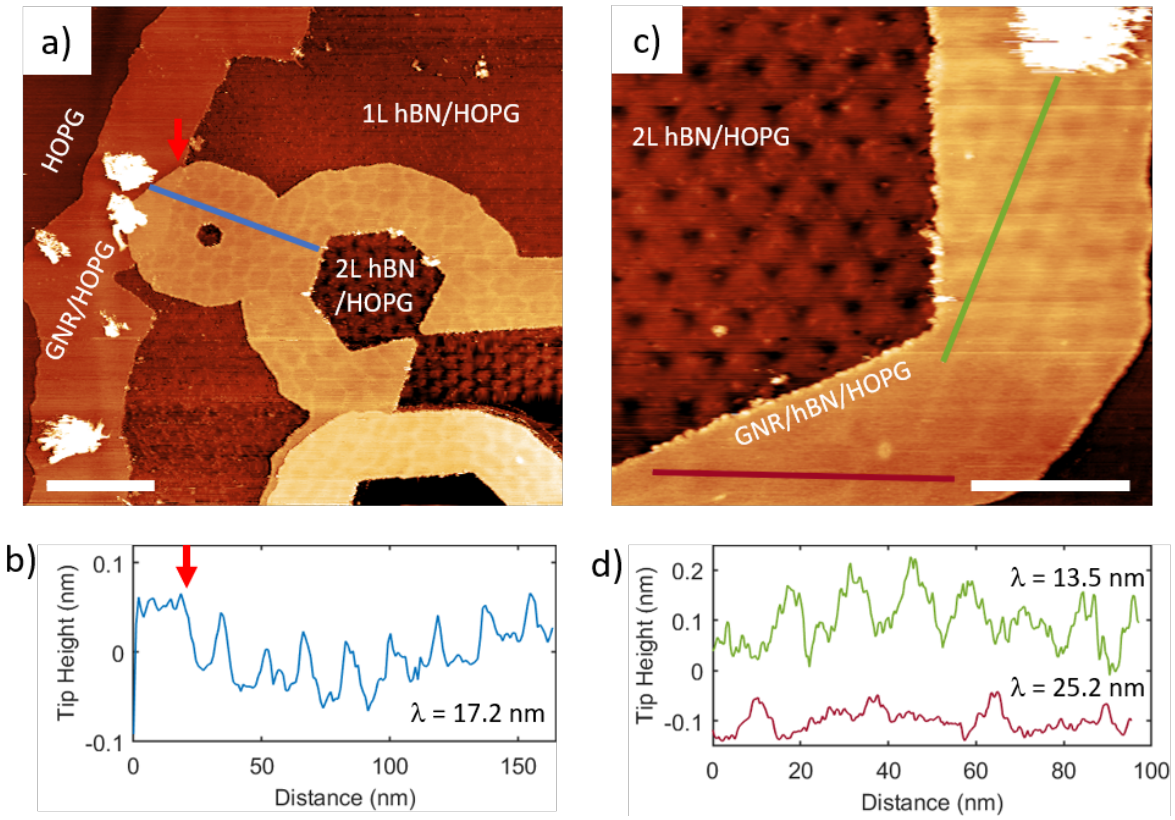

Figure 5. (a) and (c) STM images of graphene bands and graphene ribbons templated from the edges of hBN monolayers and bilayers grown by MBE on HOPG substrates. (b) and (d) STM tip height profiles measured along the associated lines drawn in (a) and (c). The scale bars are 50 nm in (a) and (c). The tunnelling parameters are (a) U_{bias} = 0.4 V; $I_{setpoint}$ = 0.3 nA, and (c) U_{bias} = 0.5 V; $I_{setpoint}$ = 0.5 nA.